AMERICAN SOCIETY FOR MICROBIOLOGY | Journal of Virology®

STRUCTURE AND ASSEMBLY

Capsid Structure of *Anabaena* Cyanophage A-1(L)

Ning Cui,[a] Feng Yang,[a] Jun-Tao Zhang,[a] Hui Sun,[a] Yu Chen,[a] Rong-Cheng Yu,[a] Zhi-Peng Chen,[a] Yong-Liang Jiang,[a] Shu-Jing Han,[a] Xudong Xu,[b] Qiong Li,[a] Cong-Zhao Zhou[a]

[a]Hefei National Laboratory for Physical Sciences at the Microscale and School of Life Sciences, University of Science and Technology of China, Hefei, Anhui, China
[b]State Key Laboratory of Freshwater Ecology and Biotechnology, Institute of Hydrobiology, Chinese Academy of Sciences, Wuhan, Hubei, China

ABSTRACT A-1(L) is a freshwater cyanophage with a contractile tail that specifically infects *Anabaena* sp. PCC 7120, one of the model strains for molecular studies of cyanobacteria. Although isolated for half a century, its structure remains unknown, which limits our understanding on the interplay between A-1(L) and its host. Here we report the 3.35 Å cryo-EM structure of A-1(L) capsid, representing the first near-atomic resolution structure of a phage capsid with a T number of 9. The major capsid gp4 proteins assemble into 91 capsomers, including 80 hexons: 20 at the center of the facet and 60 at the facet edge, in addition to 11 identical pentons. These capsomers further assemble into the icosahedral capsid, via gradually increasing curvatures. Different from the previously reported capsids of known-structure, A-1(L) adopts a noncovalent chainmail structure of capsid stabilized by two kinds of mortise-and-tenon inter-capsomer interactions: a three-layered interface at the pseudo 3-fold axis combined with the complementarity in shape and electrostatic potential around the 2-fold axis. This unique capsomer construction enables A-1(L) to possess a rigid capsid, which is solely composed of the major capsid proteins with an HK97 fold.

IMPORTANCE Cyanobacteria are the most abundant photosynthetic bacteria, contributing significantly to the biomass production, O_2 generation, and CO_2 consumption on our planet. Their community structure and homeostasis in natural aquatic ecosystems are largely regulated by the corresponding cyanophages. In this study, we solved the structure of cyanophage A-1(L) capsid at near-atomic resolution and revealed a unique capsid construction. This capsid structure provides the molecular details for better understanding the assembly of A-1(L), and a structural platform for future investigation and application of A-1(L) in combination with its host *Anabaena* sp. PCC 7120. As the first isolated freshwater cyanophage that infects the genetically tractable model cyanobacterium, A-1(L) should become an ideal template for the genetic engineering and synthetic biology studies.

KEYWORDS cyanophage, capsid, capsomer construction, cryo-EM structure

Bacteriophages are widely distributed in natural ecosystems where bacteria inhabit. With an estimated number of 10^{31} or more on the planet, phages outnumber bacteria by over 10-fold in marine and freshwater environments (1, 2). Phages that infect cyanobacteria, a large group of photosynthetic oxygenic prokaryotes, are called cyanophages (3). It has been shown that cyanophages in aquatic environments, such as oceans, rivers, and lakes, are involved in regulating the dynamics of cyanobacterial communities and successions of cyanobacterial populations (4). As autotrophic microorganisms, cyanobacteria can sequester CO_2 and generate O_2 via photosynthesis, thus playing a key role in producing the primary biomass and providing an O_2-rich atmosphere (5–7). Hence by lysing cyanobacteria, cyanophages may contribute greatly to the regulation of atmospheric levels of O_2 and CO_2, and global recycling of carbon,

Citation Cui N, Yang F, Zhang J-T, Sun H, Chen Y, Yu R-C, Chen Z-P, Jiang Y-L, Han S-J, Xu X, Li Q, Zhou C-Z. 2021. Capsid structure of *Anabaena* cyanophage A-1(L). J Virol 95: e01356-21. https://doi.org/10.1128/JVI.01356-21.

Editor Rebecca Ellis Dutch, University of Kentucky College of Medicine

Address correspondence to Xudong Xu, xux@ihb.ac.cn, Qiong Li, liqiong@ustc.edu.cn, or Cong-Zhao Zhou, zcz@ustc.edu.cn.

Received 12 August 2021
Accepted 19 September 2021
Accepted manuscript posted online 22 September 2021
Published 23 November 2021

nitrogen as well (8–11). Moreover, they could cause the collapse of cyanobacterial blooms, thus might be developed into potential biological agents for the control of seasonal outbreak of cyanobacteria (12, 13). Based on tail morphology, cyanophages are usually categorized within three families, namely, the *Podoviridae* (short tail), *Siphoviridae* (long noncontractile and flexible tail) and *Myoviridae* (long contractile tail, with a central tube surrounded by a contractile sheath), all of which belong to the *Caudovirales*—tailed double-stranded DNA (dsDNA) bacteriophages (14). However, the latest classification of International Committee on Taxonomy of Viruses (ICTV) shows that some cyanophages infecting *Synechococcus* and *Prochlorococcus* belong to the *Autographiviridae* family (15). In addition, recent reports also indicated the existence of tailless cyanophages (16, 17).

Anabaena sp. PCC 7120 (here *Anabaena* 7120) is a freshwater filamentous nitrogen-fixing cyanobacterium (18). It has long been utilized as a model organism to study the genetics and physiology of bacterial cell differentiation and nitrogen fixation (19). In this strain, highly efficient genetic tools have been developed, including gene transfer based on conjugation (20) or electroporation (21), selection of homologous recombinants based on *sacB* (22) or CpfI (23), and transposon mutagenesis (24). Potentially, *Anabaena* 7120 may also be developed into a model strain for studies of its interplay with cyanophages. *Anabaena* 7120 can be infected and lysed by the cyanophages *Myoviridae* A-1(L) and *Podoviridae* A-4(L), where the letter "L" designates the sample isolation place—Leningrad (25). Of the two cyanophages, A-1(L) has a icosahedral capsid of 66 $\pm$ 4 nm in diameter, connected to a contractile tail of 118 $\pm$ 6 nm in length (26). Moreover, A-1(L) possesses a 68,304 bp genome with 97 putative open reading frames, including a DNA polymerase B with high similarity to that encoded by *Anabaena* 7120, suggesting a long history of phage-host coevolution (27). The infection of A-1(L) toward *Anabaena* 7120 depends on the specific interaction between the phage tail protein and host lipopolysaccharide (28). Beyond this, we know very little about how A-1(L) interplays with *Anabaena* 7120 in the life cycle of virus from infection, replication, propagation to release.

Like *Siphoviridae* phages, the capsid, tail, and tail fibers of *Myoviridae* phages are assembled independently, and are subsequently joined together to form a mature virion (29, 30). Most tailed dsDNA phages have an icosahedral capsid, which is usually composed of a major capsid protein with an HK97 fold (31). Due to the plasticity of the P-domain, E-loop and A-domain, the major capsid protein subunits are able to be organized into pentons and hexons with different curvatures. The pentons and/or hexons (capsomers) are further interlocked via diverse interfaces to form the icosahedral capsid (32). In some cases, extra cement proteins or so-called auxiliary proteins are recruited at 2-fold or 3-fold axes of the capsid, to further reinforce the capsid stability (33–36).

To understand how cyanophages interplay with their hosts, it is important to establish cyanophage-host model systems to perform in-depth molecular studies. A-1(L) and *Anabaena* 7120 could be a promising candidate system. To this end, we need to have the structure information of A-1(L), beyond the present efficient genetic tools established in *Anabaena* 7120. Here we employed the cryogenic electron microscopy (cryo-EM) method to solve the structure of A-1(L) capsid at near-atomic resolution, and revealed a unique capsomer construction of the capsid.

RESULTS

Overall structure of A-1(L) capsid. Using CsCl density gradient centrifugation, we purified the viral particles of A-1(L) and applied the frozen-hydrated samples to cryo-EM. The recorded cryo-EM images showed that the A-1(L) virion possesses an icosahedral head with a diameter of ~740 Å, and a stretched tail of ~1,200 Å in length (Fig. 1A), which is generally in agreement with the previous measurement by negative-staining EM (26). The capsid structure of A-1(L) was reconstructed with 32,687 viral particles from a total of 4,484 frames, and finally determined to an overall resolution of

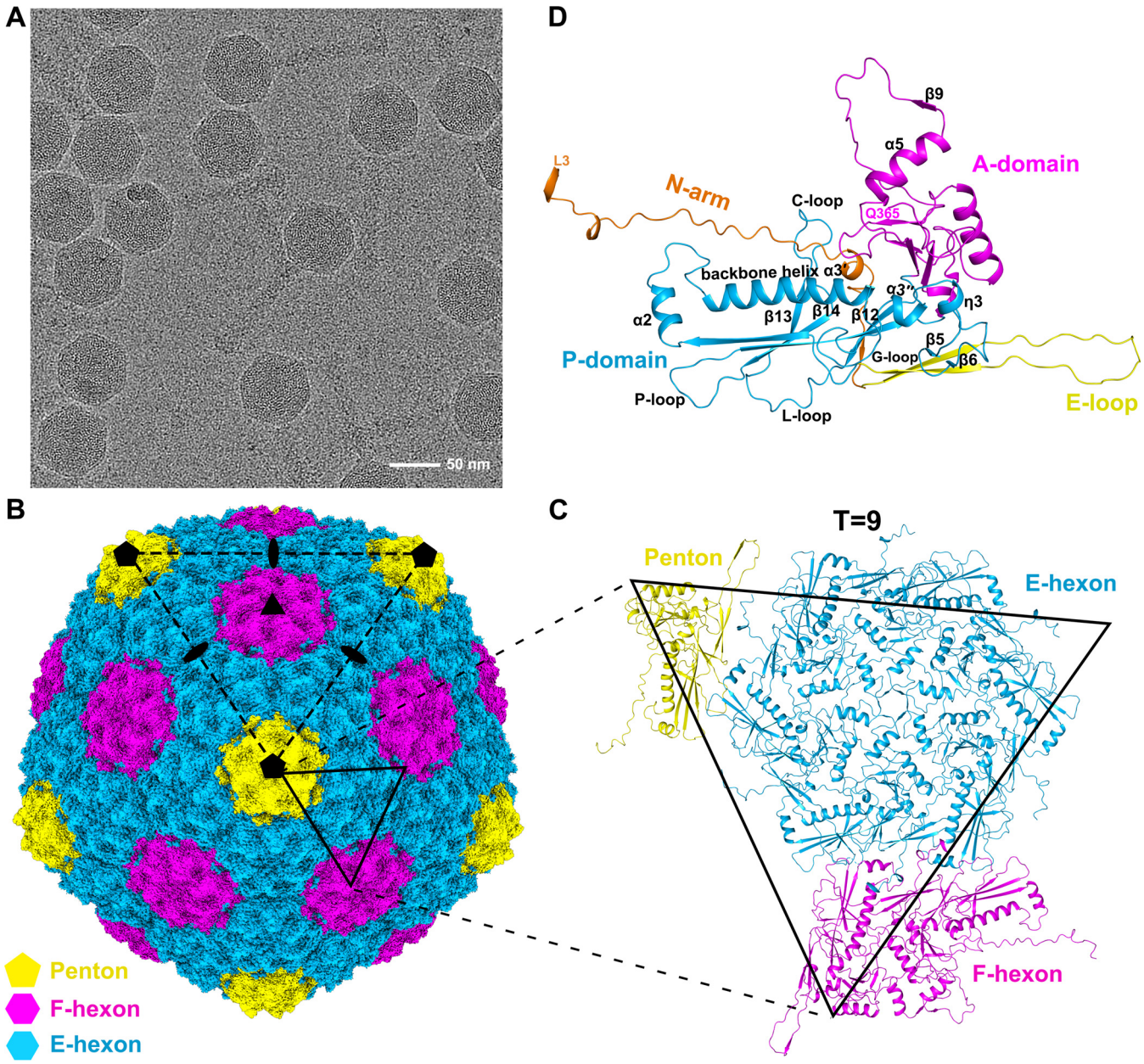

FIG 1 Structure of A-1(L) capsid. (A) A representative cryo-EM image of A-1(L). The scale bar represents 50 nm. (B) Surface presentation of the overall structure of the A-1(L) capsid. The penton, F-hexon, and E-hexon are colored in yellow, magenta, and sky blue, respectively. The dashed-line triangle represents a triangular facet of icosahedron, whereas the solid-line triangle shows an asymmetric unit. The small black triangles, long ovals, and pentagons represent the 3-, 2- and 5-fold axes, respectively. (C) Cartoon presentation of an asymmetric unit of A-1(L) capsid. (D) Overall structure of the major capsid protein gp4. The four discrete domains are labeled and differentially colored.

3.35 Å. Afterward, the molecular model of the major capsid protein gp4 was built *de novo*, in which the side chains of most residues well matched the densities. Notably, no cement protein could be assigned in the density map, which is consistent with the genomic analysis (27).

In total, the isometric capsid shell of A-1(L) consists of 535 copies of gp4, forming 80 hexons and 11 pentons (Fig. 1B). According to the shape and localization, 80 hexons could be further classified into two types: 20 at the center of the facet and 60 at the facet edge, named F-hexon and E-hexon, respectively. The F-hexon (colored in magenta) is located at the center of each triangular facet surrounding the 3-fold symmetry axis, whereas two E-hexons (colored in sky blue) and two pentons (colored in yellow) constitute an edge of the icosahedron (Fig. 1B).

Structural analysis showed that the capsid of A-1(L) exhibits a triangulation number T of 9, corresponding to each icosahedral asymmetric unit composed of nine gp4 subunits: eight hexameric subunits of two adjacent hexons and one pentameric subunit (Fig. 1C). In contrast to the relatively popular symmetry mode of T = 7 (34, 37–42), or T = 13 (36, 43, 44), only a few cases of T = 9 have been reported (45–47). However, due to the limited resolution, the fine capsid construction with a T number of 9 remains unknown.

The major capsid protein gp4. The atomic model of the major capsid protein gp4 in the hexons was built from the residue Leu3 to Asn365 (out of 365 residues); however, a segment from the residue Asp312 to Ser321 is missing in the pentons. Each gp4 subunit is composed of four domains: an elongated N-terminal arm (N-arm), an extended loop (E-loop), a peripheral domain (P-domain), in addition to an axial domain (A-domain) at the center of each capsomer (Fig. 1D). Although sharing a low primary sequence identity, the overall structure of gp4 resembles the canonical HK97 fold, which has been found in the major capsid proteins of tailed dsDNA bacteriophages and herpesviruses (37, 48, 49). The backbone helix α3, a characteristic feature of the HK97 fold, is also split into two parts (α3′ and α3′′) by a G-loop that named after its conserved glycine residues (Fig. 1D).

The major capsid protein gp5 of HK97 (PDB: 1OHG) represents the most classical and simplest example of the capsid structure in tailed dsDNA phages (37). Structural comparison of A-1(L) gp4 against HK97 gp5 yielded an overall root-mean-square deviation (RMSD) of 3.12 Å over 229 Cα atoms (Fig. 2A). Two main structural differences were found: (i) the helix η3 and β-turn-β hairpin (β5-β6) between the P-domain backbone helix α3 and A-domain, protruding outward from the surface of capsid; (ii) two loops located at the inner surface of capsid shell. The two loops—one between β12 and β13 (termed L-loop), the other between β13 and β14 (termed C-loop)—are formed due to an extra strand β13, which is absent in gp5 of HK97 (Fig. 1D and 2A). Similarly, an extra β strand also exists in the major capsid protein gp5 of Sf6 (PDB: 5L35) (40), resulting in a similar L-loop, but a much shorter C-loop (Fig. 2B). In addition, DALI search (50) revealed that gp4 is most similar to the major capsid protein gp40 of cyanophage Mic1 (PDB: 6J3Q), with an RMSD of 2.4 Å over 313 Cα atoms and a sequence identity of 20% (36). However, gp40 of Mic1 possesses an additional insertion domain, whereas gp4 of A-1(L) has an extra strand β13 (Fig. 2C). These structural differences suggest that A-1(L) might adopt a unique capsid construction different from the previously reported bacteriophages.

In contrast to eight hexameric gp4 subunits of an asymmetric unit that are structurally similar to each other with an RMSD of 0.55∼1.16 Å, the pentameric gp4 subunit differs a lot with those hexameric subunits in structure with an RMSD of 1.44∼1.69 Å. First, the elongated N-arms within the eight hexameric gp4 subunits swing from each other up to ∼9°; and the most distal one further swings ∼13° from the hexameric to pentameric gp4 subunit, resulting in a maximum shift of ∼20 Å for the N-terminal residue Leu3 (Fig. 2D). Second, compared to the hexameric gp4 subunits, the distal loops of A-domain and E-loop of pentameric gp4 undergo a significantly tilt of ∼75° and ∼20°, thus shift ∼26 Å and ∼11 Å toward the interior of the capsid shell, respectively (Fig. 2D). Third, helix α2 of pentameric gp4 P-domain also tilts ∼12° with a positional displacement of ∼6.4 Å (Fig. 2D). The C-loop was not defined in the pentameric gp4 subunits due to the poor cryo-EM density, suggesting that this loop is relatively flexible. Altogether, the variations of these structural elements enable the oligomerization of gp4 subunits into both pentons and hexons, which further constitute the icosahedral capsid shell.

The penton and two variable hexons. Mainly via the crossed A-domains at the center and the "head-to-tail" interactions between P-domains and adjacent E-loops at the periphery, the major capsid proteins assemble into the penton and two variable hexons: F-hexon and E-hexon. Although F-hexon and E-hexon share an approximately same diameter of ∼152 Å, they possess a rather different thickness of 39 and 42 Å, respectively (Fig. 3A). Moreover, despite slight structural variations in each subunit of gp4 hexon (Fig. 2D), the overall structures of F-hexon and E-hexon differ significantly.

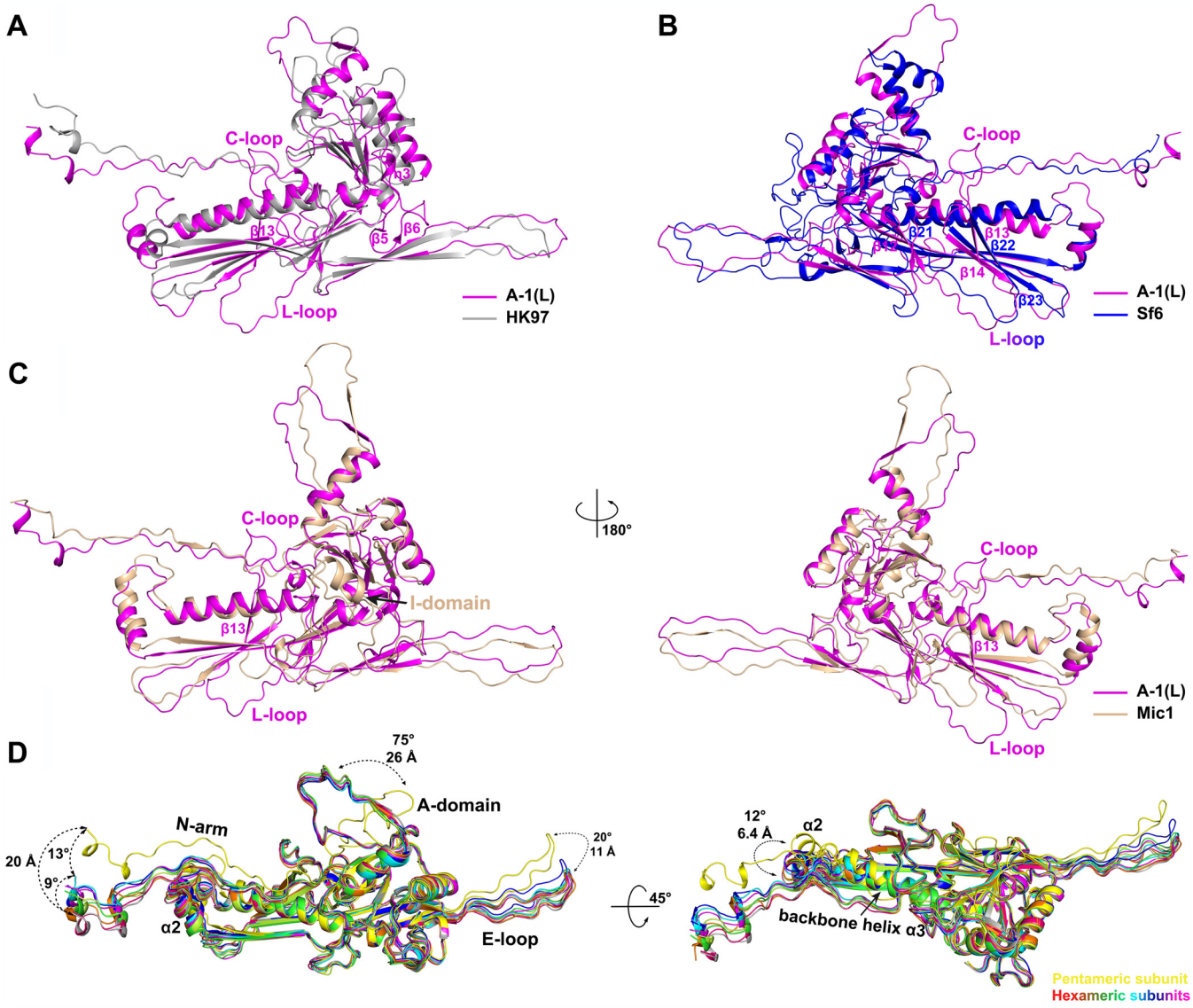

FIG 2 Conformational flexibilities of the major capsid protein gp4. (A) Structural superposition of the A-1(L) gp4 (magenta) against the HK97 major capsid protein gp5 (gray, PDB: 1OHG). The secondary structure elements (β13, C-loop, L-loop, η3, β5 and β6) distinct from those of HK97 are labeled. (B) Structural superposition of the A-1(L) gp4 (magenta) against the Sf6 major capsid protein gp5 (blue, PDB: 5L35). The two loops and related β strands are labeled. (C) Structural superposition of the A-1(L) gp4 (magenta) against the Mic1 major capsid protein gp40 (wheat, PDB: 6J3Q). The insertion domain (I-domain) of Mic1 gp40 is labeled. (D) Structural superposition of nine gp4 subunits within an asymmetric unit. The pentameric subunit is colored in yellow, whereas the hexameric subunits are shown in multiple colors. The significant structural variations are labeled.

When the A-domains at the center were aligned, structural superposition revealed the P-domain at the periphery of one subunit in E-hexon bends ~9.5° compared to that in F-hexon (Fig. 3B). In consequence, the most distal atom (Cα atom of the residue Glu333) from the E-hexon center shifts ~12.1 Å inward the capsid (Fig. 3B), resulting in an increased curvature of E-hexon in comparison to F-hexon.

In contrast to the hexons, pentons possess a much smaller diameter of 128 Å, accompanied by an increased thickness of 52 Å (Fig. 3A), forming a convex surface bulging outward on the capsid. The plasticity of individual gp4 subunits in hexon and penton, including the N-arm, the distal loops of A-domain and E-loop, the helix α2 (Fig. 2D), together contribute to the dramatic changes in curvature of the penton compared to that of E-hexon. Beyond the increase in curvature, the ~75° tilt of the A-domain distal loop, induced by the helix-to-loop transition of helix α5, also leads to the enlargement of the central pore diameter from 6.1 Å in the E-hexon to 8.0 Å in the penton. Moreover, the increased curvature might also result in higher flexibility of

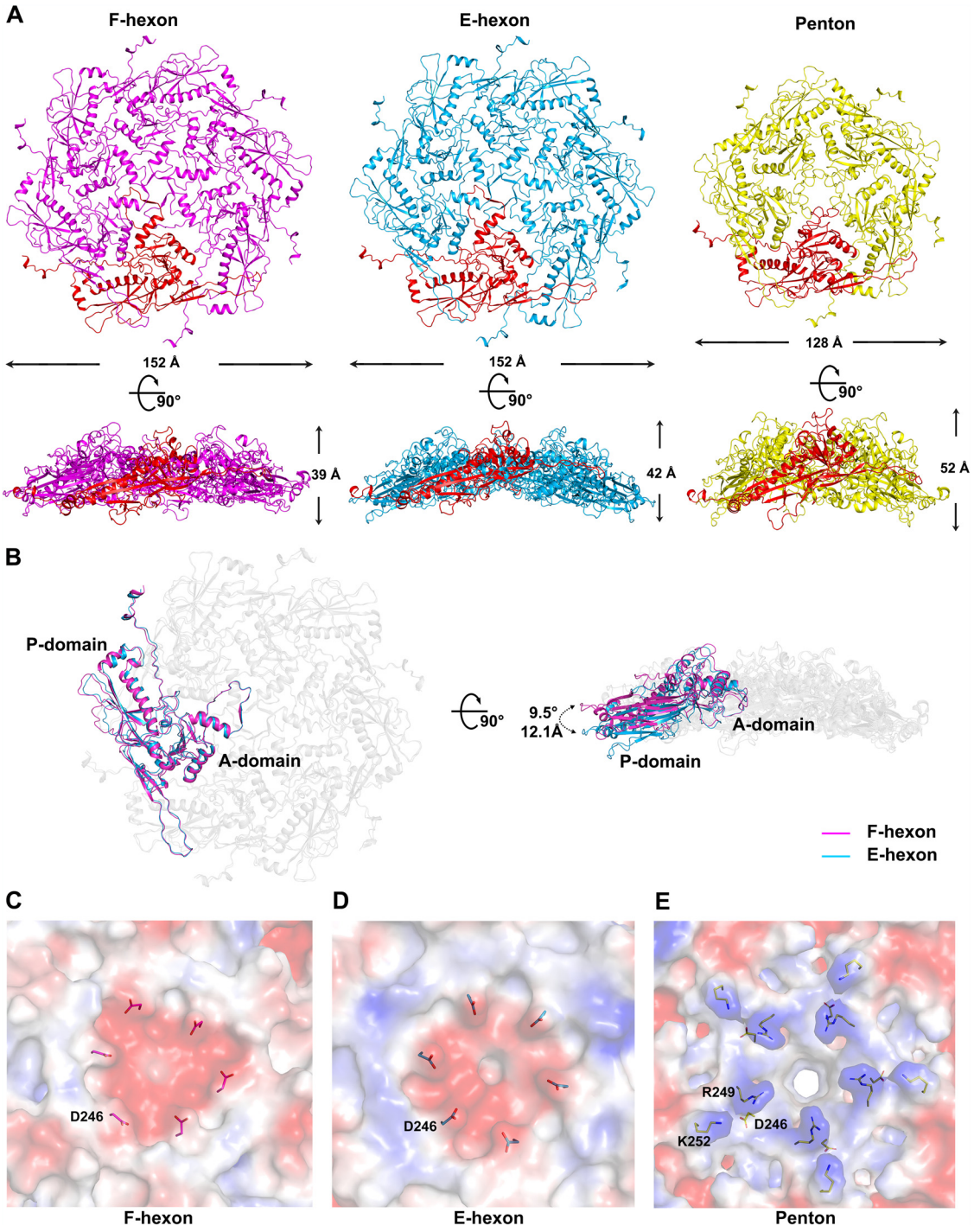

FIG 3 Structures of the penton and two types of hexon. (A) Cartoon presentations of the F-hexon (five subunits in magenta and one subunit in red), the E-hexon (five subunits in sky blue and one subunit in red) and the penton (four subunits in yellow and one subunit in red) of A-1(L), shown in top and side views, respectively. (B) Superposition of the F-hexon (magenta) against E-hexon (sky blue), shown in top and side views, respectively. The aligned subunit is shown as magenta and sky blue cartoon, respectively, whereas the remaining subunits are shown as semitransparent cartoon. The charged residues, shown as sticks, contribute to the electrostatic potential at the central pores of (C) F-hexon, (D) E-hexon and (E) penton.

the C-loop, which is missing in the structure of the penton. Thus, we propose that the F-hexon, E-hexon and penton capsomers employ gradually increasing curvatures to finely fit the shape of icosahedral capsid, especially at the vertex.

In addition, although the F-hexon, E-hexon and penton all harbor a discrete but regular distribution of electrostatic potential at the inner surface, the central pores are

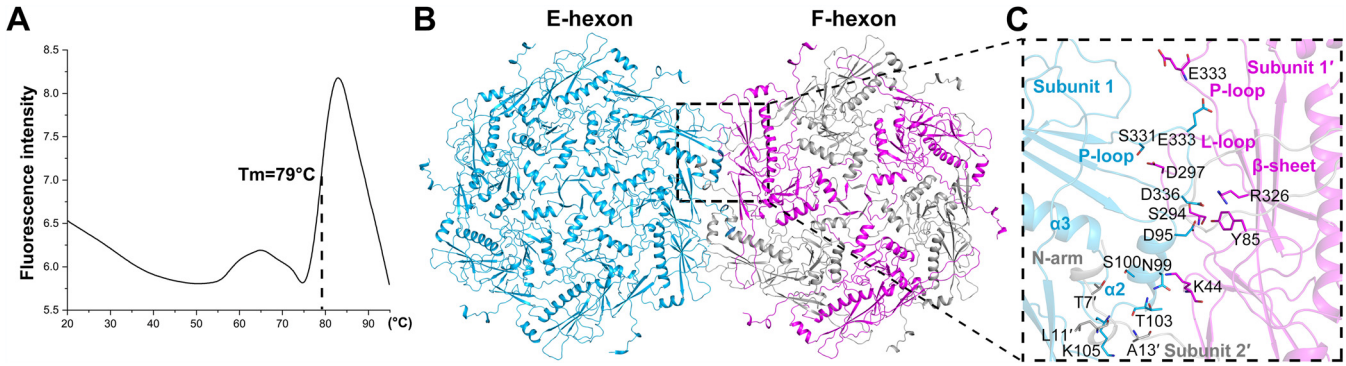

FIG 4 The T_m value and structural complementarity between the F-hexon and E-hexon at the 2-fold axis. (A) The T_m curve of A-1(L), calculated by the thermal shift assay. (B) An exterior view of the interface is shown as cartoon, with (C) a zoom-in view shown as an inset. One subunit of E-hexon (sky blue) interacts with two subunits of F-hexon (magenta and gray). The residues forming hydrogen bonds and salt bridges are shown as sticks, colored the same as the cartoon presentation, and labeled.

charged differently. In contrast to both F-hexon and E-hexon, which are negatively charged at the inner central pore (Fig. 3C and D), the penton is positively charged (Fig. 3E). This structural variation in charge is due to the clustering of the basic residues Arg249 and Lys252 surrounding the central pore, accompanied by the outward shift of acidic residue Asp246 at the distal loop of A-domain in the penton (Fig. 3E).

Construction of A-1(L) capsid. Despite being solely composed of major capsid proteins gp4 of an HK97 fold, A-1(L) possesses a rather high denaturation temperature (T_m) at ~79°C (Fig. 4A), comparable to the previously reported cyanophage Mic1 that is stabilized by cement proteins (36). This rigid capsid of A-1(L) is constituted by interlocked capsomers via mutually intervening structural elements of gp4.

Around the 2-fold axis, the E-hexon interacts with the neighboring F-hexon, E-hexon and penton, forming three interfaces (Fig. 1B and 4B). In detail, the helix α2 and P-loop at the P-domain of subunit 1 of E-hexon mainly interact with the P-domain (P-loop, L-loop and four-stranded β-sheet) and N-terminus of E-loop (residue Lys44) of subunit 1′ of F-hexon via seven pairs of inter-capsomer hydrogen bonds (Fig. 4C). Moreover, residues Thr7′, Leu11′ and Ala13′ at the N-arm of adjacent subunit 2′ in F-hexon form hydrogen bonds with residues Ser100, Lys105 and Thr103 located at helix α2 and the succeeding loop$_{\alpha2\text{-}\alpha3}$ of the P-domain of subunit 1 of E-hexon (Fig. 4C), to further stabilize the interface. In addition, this interface also displays complementary electrostatic interactions: the negatively charged helix α2 and P-loop at the P-domain of subunit 1 of E-hexon insert into a positively charged groove of F-hexon, which is formed by the P-domain of subunit 1′ and the N-arm of adjacent subunit 2′. Notably, the E-hexon forms an interface with the neighboring E-hexon and the penton, respectively, similar to that between the E-hexon and F-hexon.

At the pseudo 3-fold axis, A-1(L) capsid also adopts a chainmail structure, of which the so-called metacapsomers are interlocked (Fig. 5A and B). The metacapsomer refers to metapenton or metahexon, which is composed of a penton and its five surrounding hexons, or a hexon and its six surrounding hexons (or a hexon and its five surrounding hexons and one surrounding penton), respectively. The P-domains and E-loops of five or six gp4 subunits that closely surround the central penton or hexon of the metacapsomer, interact with each other in a "head-to-tail" manner to form a 5-fold or 6-fold symmetric ring (colored the same in Fig. 5A). The neighboring rings cross each other to form an interlocked chainmail structure.

Different from the covalent bonding in HK97 (37) or strong electrostatic interactions in BPP-1 (34), the A-1(L) capsid adopts a three-layered interface among metacapsomers via hydrogen bonds and salt bridges (Fig. 5B and C), adopting a noncovalent chainmail structure. The three layers at the interface are respectively formed by the L-loops, P-loops and E-loops from three adjacent hexons, which are stacked against each other around the pseudo 3-fold axis (Fig. 5C and D). The three L-loops from subunits 2, 4 and 6 of three adjacent

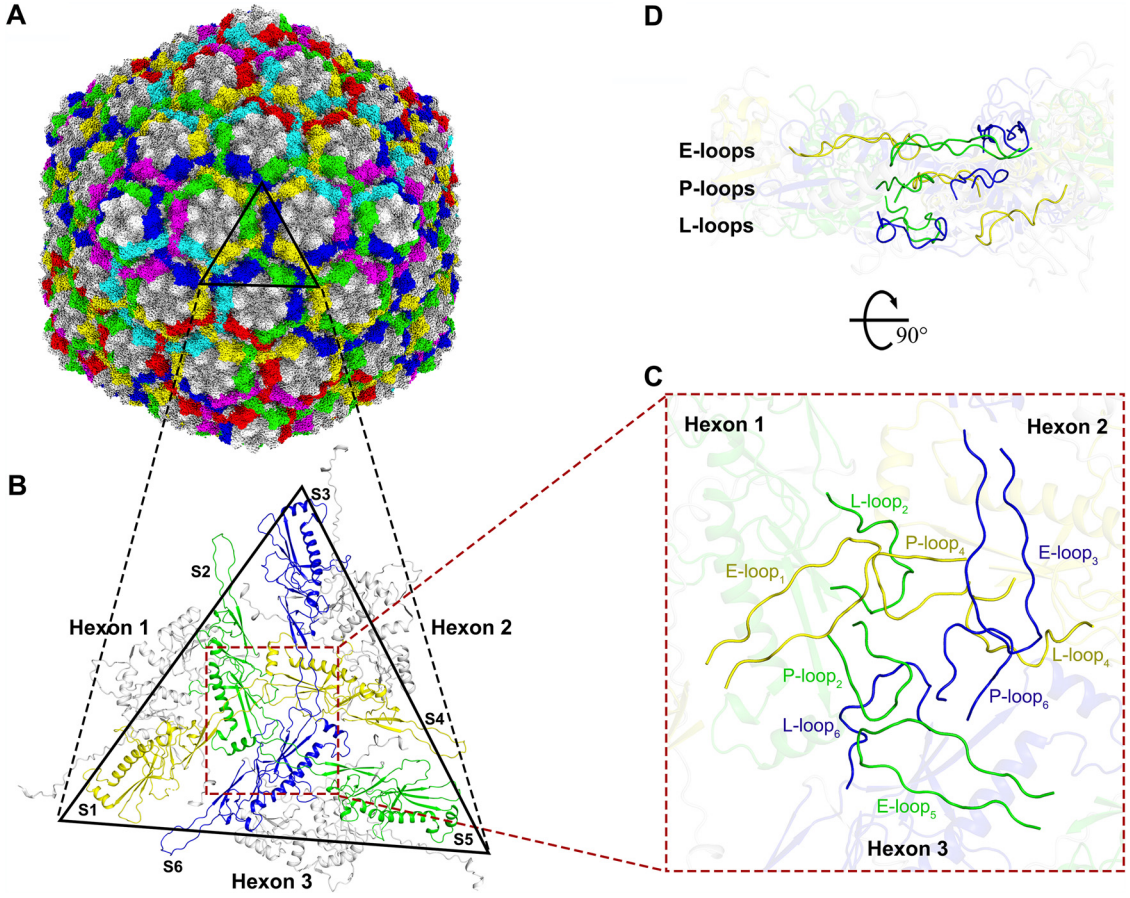

FIG 5 The noncovalent chainmail structure of A-1(L) with a three-layered interface. (A) The noncovalent chainmail structure of A-1(L) capsid. The P-domains and E-loops of gp4 subunits involved in the formation of one metacapsomer are shown in the same color, whereas other regions are colored in gray. (B) A closeup view of the three-layered interface between three hexons, colored the same as the overall chainmail structure. Three L-loops and three P-loops of subunits 2, 4 and 6, three E-loops of subunits 1, 3, and 5, constitute the innermost, middle, and outermost layers, respectively. The interface is shown in (C) top and (D) side views, respectively.

hexons constitute the innermost layer of the interface, whereas three P-loops from the corresponding three subunits form the middle layer. Although the three L-loops do not interact with each other, each L-loop interacts with the P-loop and its N-terminal β strand of the same subunit by three pairs of hydrogen bonds (Gln293-Arg326, Lys302-Asp329 and Thr304-Leu327). Moreover, three P-loops are pairwise connected via salt bridges to further stabilize the interface. At the outermost layer, three E-loops from subunits 1, 3 and 5 stick on the middle-layered P-loops of subunits 4, 6 and 2 from the same metacapsomer, respectively (Fig. 5C and D). Residues Gly64 and Arg60 of the E-loop form hydrogen bonds with residues His334 and Asp336 of the P-loop, in addition to a pair of salt bridge between Arg60 of the E-loop and Glu341 of the P-loop from the adjacent metacapsomer. Similarly, a penton and two neighboring hexons also adopt a noncovalent chainmail junction with a same three-layered interface.

Altogether, these unique three-layered interfaces at the pseudo 3-fold axes of metacapsomers, in combination with the complementarity in shape and electrostatic potential at the interfaces of capsomers around the 2-fold axes, are strongly reminiscent of a fine mortise-and-tenon construction, which would greatly augment the stability of the icosahedral A-1(L) capsid.

DISCUSSION

The first high-resolution structure of a bacteriophage capsid was solved at 3.6 Å resolution using crystallography, namely, the HK97 empty capsid (37). Afterward, thanks to the

revolutionary progress of cryo-EM, a series of near-atomic resolution structures of phage capsids were determined (39, 51, 52). These structures suggested that the canonical HK97 fold appears to be very popular in the capsids of tailed dsDNA phages, even in the lower domains of the herpesviruses' major capsid proteins (49). During assembly, major capsid proteins are programmed by the scaffolding proteins to form multiple copies of capsomers, and the inter- and intra- capsomer interactions that largely contribute to the 3-D arrangement and stability of capsid (53, 54). Although the HK97 fold is common and conserved, the construction of capsid varies considerably, mainly due to the insertion domains in the HK97 fold and/or the additional cement proteins (also termed decoration proteins or auxiliary proteins) that anchor on the capsid.

Many tailed dsDNA bacteriophages have the major capsid proteins that adopt an HK97 fold and possess an insertion domain. In the cases such as bacteriophages P22, T7 and Sf6, the insertion domain of major capsid protein contributes to the stability of phage capsid via forming noncovalent chainmail structure (40, 55). In this study, we solved the capsid structure of the freshwater cyanophage A-1(L), revealing an HK97-fold major capsid protein gp4 without an insertion domain (Fig. 1D). Notably, the phages that possess the major capsid proteins without an insertion domain, such as T5 and TW1, usually utilize the extra cement proteins to stabilize the capsid (41, 56). However, the capsid of A-1(L) is solely composed of the major capsid proteins gp4, without any cement proteins (Fig. 1B). Together, it suggested that A-1(L) might possess a distinct capsid assembly pattern.

To date, most tailed dsDNA phage capsids that have been studied in detail, have an icosahedral geometry of T = 7 or 13 (34, 36–44, 53, 57–61), with a few exhibiting larger capsids with a T number of 16 or more (62–67). The capsid structure of A-1(L) represents the first structure of phage capsid with a T number of 9 at near-atomic resolution. In previous reports (36, 39, 42, 44), phage capsids with a T = 7 geometry could only accommodate one type of penton and one type of hexon, whereas those with a T = 13 usually consist of one type of penton and two types of hexons. For example, in the case of the Mic1 capsid with a T = 13 geometry, three central hexons are located at each triangular facet, and two peripentonal hexons are asymmetrically situated at the edge of icosahedron (36). The A-1(L) capsid with a T = 9 geometry also possesses one type of penton and two types of hexons; however, the capsomers are assembled in a different pattern: one F-hexon located at the center of each triangular facet and two E-hexons symmetrically aligned at the edge of icosahedron (Fig. 1B). Thanks to the gradually increasing curvatures, these capsomers could perfectly assemble into the icosahedral capsid structure of A-1(L).

Icosahedral capsids of tailed bacteriophages need to withstand not only wide ranges of environmental stresses, but also internal pressures exerted by the encapsulated dsDNA genome, for survival and propagation (68). Accordingly, they evolved a highly stable protein chainmail structure, formed by intervened rings with five or six major capsid protein subunits, to maintain the structural integrity and rigidity of capsids (55). The chainmail structure was first discovered in HK97 (69), and observed afterward in many dsDNA viruses, such as P22 (70), BPP-1 (34), λ (57) and herpesviruses (49, 71). The HK97 capsid mainly utilizes unique isopeptide bonds to maintain the stability of protein rings at the pseudo 3-fold axes, representing the only known structure of a covalent-bonded chainmail (37). For P22, the D-loop of the insertion domain in major capsid protein subunit is used to form a noncovalent chainmail structure via polar interactions across 2-fold axes of symmetry (55, 72). The BPP-1 capsid is stabilized by dimeric cement proteins at the 2-fold interface (34), whereas the λ phage employs a trimeric cement protein to stabilize the capsid at the 3-fold axis (57). In contrast, A-1(L) adopts a three-layered interface at the pseudo 3-fold axis via hydrogen bonds and salt bridges, in combination with the complementarity in shape and electrostatic potential around the 2-fold axis (Fig. 4 and 5), to reinforce the stability of capsid. Compared to the common double-layered interface (P-loops and E-loops) at the 3-fold axis (36, 37, 53, 56), A-1(L) employs three additional L-loops from the adjacent capsomers to constitute an extra layer of interface at the innermost. Moreover, A-1(L) shows a relatively high

TABLE 1 Cryo-EM parameters, data collection, refinement statistics

Data collection and processing	A-1(L) Capsid (PDB 7F38) (EMD-31431)
Magnification	26,000
Voltage (keV)	300
Electron exposure (e^{-}/Å^2)	50
Defocus range (μm)	1.5∼2.5
Pixel size (Å)	1.22
Symmetry imposed	I3
Initial particle images (no.)	38,857
Final particle images (no.)	32,687
Map resolution (Å)	3.35
FSC threshold	0.143
Map resolution range (Å)	2.44∼999
Refinement	
Real-space correlation coefficient	0.8189
Initial model used (PDB code)	*ab-initio*
Map sharpening B factor (Å^2)	-112.347
Model composition	
Nonhydrogen atoms	1,488,300
Protein residues	195,420
Waters	0
RMS deviation from ideality	
Bond lengths (Å)	0.009
Bond angles (°)	0.861
Validation	
MolProbity score	2.57
Clash score	28.06
Poor rotamers (%)	0.04
Ramachandran statistics	
Favored regions (%)	86.15
Allowed regions (%)	13.79
Outliers (%)	0.06

T_m up to ∼79°C (Fig. 4A), comparable to that of Mic1. Although Mic1 only has a classical double-layered interface at the 3-fold axis of capsid, it possesses the cement proteins anchoring on the capsid to stabilize the capsid (36). Based on these analyses, we propose that A-1(L) capsid utilizes a novel noncovalent chainmail structure with mortise-and-tenon junctions, distinct from other HK97 type capsids of bacteriophages.

To date, two structures of marine cyanophages P-SSP7 and Syn5, in addition to one structure of a freshwater cyanophage Mic1, have been reported at 4.6, 4.7, and 3.5 Å resolution, respectively (36, 59, 60). The present structure of A-1(L) capsid represents the first structure for a cyanophage that infects a freshwater and genetic tractable model cyanobacterium. With this capsid structure, and hopefully the intact viral structure of A-1(L) in the future, the structure-function relationships and interplays between A-1(L) and its host could be further investigated in *Anabaena* 7120 by genetic modifications of both cyanophage and cyanobacterium.

MATERIALS AND METHODS

A-1(L) purification. The *Anabaena* 7120 cells were grown in BG11 at 30°C under a light intensity of 2,000 lux to an $OD_{730\ nm}$ of 0.7. A-1(L) at a multiplicity of infection of ∼0.01 was added to the culture. After infection, cell lysate was centrifuged first to remove the cellular debris, then 1 μg/ml DNase I and RNase A were added to the supernatant and incubated at 25°C for 2 h. Afterward, A-1(L) virions were collected by centrifuging at 8,000 g for 16 h at 4°C. The pellet containing A-1(L) was resuspended in SM buffer (50 mM Tris, pH 7.5, 100 mM NaCl, 10 mM $MgSO_4$). The suspension was loaded onto a discrete CsCl density gradient (1.30, 1.35, 1.40, 1.45, 1.50 g/ml), and further centrifuged at 100,000 g for 4 h at 4°C using SW 40 Ti rotor (Beckman Coulter). After centrifugation, the band corresponding to A-1(L) was collected and dialyzed against SM buffer at 4°C overnight to remove CsCl.

Cryo-EM sample preparation. The purified A-1(L) particles were concentrated using an ultracentrifugal filter with a 100-kDa cutoff (Amicon; EMD Millipore, Billerica, MA, USA). The negative-staining EM was used to check the purity and integrity of A-1(L) viral particles. A sample of 3.5 μl of concentrated A-1(L) particles was loaded onto a R2/1 300-mesh cooper grid (Quantifoil), which has been plasma cleaned for 10 s in a plastic cleaner. The grid was then blotted with GE filter paper for 3 s in 100% relative humidity with a blot force of −2, plunged into liquid ethane, and transferred into a holder to store the specimen in liquid nitrogen.

Cryo-EM data collection and processing. Cryo-EM movies (40 frames, each 0.15 sec) were recorded at nominal magnification of 22,600× on a FEI Titan Krios electron microscope operated at 300 kV. The total accumulated dose is 50 e-/Å^2, And the final pixel size is 1.22 Å. The defocus range is 1.5 ~2.5 μm. Totally, 4,484 micrographs were recorded. The movie frames were motion corrected and dose weighted using MotionCor2 (73), and the defocus were determined by CtfFind4 (74).

To determine the capsid structure of A-1(L), a total of 38,857 particles were selected and extracted by RELION3.1 (75). All extracted particles were applied to 2D classification, and then all good subsets were selected and subjected to 3D reconstructions. After several iterations of 2D and 3D classifications, 32,687 particles were used to do the 3D refinement, yielding a final reconstruction map at 3.35 Å according to the Gold standard Fourier shell correlation using the 0.143 threshold.

Model building and refinement. The high quality of cryo-EM map enables us to *de novo* build the atomic model of one gp4 subunit with Coot (76). Then the model was iteratively adjusted by several rounds of automatic refinement in Phenix.real-space refinement (77) and manually refinement in Coot (76). The final model was evaluated by Molprobity (78).

Afterward, one gp4 subunit was individually fitted into the density of an asymmetric unit comprising nine gp4 subunits. Then each gp4 subunit in an asymmetric unit, especially for the variable regions (N-arm, distal loop in A-domain and E-loop) were manually adjusted and refined with Coot (76). Afterward, the model of an asymmetric unit was applied to the automatic refinement by Phenix.real-space refinement. Then the whole viral capsid was built with the refined asymmetric unit by imposing icosahedral symmetry I3 using Chimera (79). The cryo-EM parameters, data collection and refinement statistics were summarized in Table 1. The structure figures were prepared using Chimera (79), ChimeraX (80) and PyMOL (www.pymol.org). The interactions between the capsomers were analyzed using PDBsum (81) and PISA server (82) at the European Bioinformatics Institute.

Thermal shift assay. Thermal shift assay measures the fluorescence emission upon binding of a probe to an exposed hydrophobic region, after heating to denature the protein. It was used to determine the T_m of A-1(L). Thermal shift assays were performed with purified A-1(L) particles and 5×SYPRO Orange (Sigma) in a volume of 10 μl. Melting curve was measured with the temperature range from 20°C to 95°C via a real-time qPCR machine. The T_m value was obtained by fitting the melting curve with a sigmoid equation.

Data availability. The structure of A-1(L) capsid has been deposited in the Protein Data Bank (PDB ID: 7F38). The cryo-EM density map has been deposited in the Electron Microscopy Data Bank (EMD-31431).

ACKNOWLEDGMENTS

We thank Dr. Yong-Xiang Gao for technical support on cryo-EM data collection of A-1(L) at the Center for Integrative Imaging of Hefei National Laboratory for Physical Sciences at the Microscale, University of Science and Technology of China.

This research was supported by the Ministry of Science and Technology of China (grant no. 2018YFA0903100), the National Natural Science Foundation of China (grant no. U19A2020) and the Fundamental Research Funds for the Central Universities (grant no. WK9100000015).

We declare that we have no competing interests.

Cong-Zhao Zhou, Qiong Li, and Xudong Xu conceived, designed, and supervised the project. Ning Cui, Qiong Li, and Cong-Zhao Zhou analyzed the data. Ning Cui, Xudong Xu, Qiong Li, and Cong-Zhao Zhou wrote and revised the manuscript. Ning Cui, Rong-Cheng Yu, Hui Sun, and Shu-Jing Han performed A-1(L) purification. Ning Cui, Feng Yang, Jun-Tao Zhang, Yu Chen, Zhi-Peng Chen, Yong-Liang Jiang, and Qiong Li performed the cryo-EM sample preparation, data acquisition, structure determination, model building, and model refinement. Xudong Xu provided the original A-1(L) virion. All of the authors discussed the data and read the manuscript.

REFERENCES

1. Hendrix RW. 2003. Bacteriophage genomics. Curr Opin Microbiol 6:506–511. https://doi.org/10.1016/j.mib.2003.09.004.
2. Parikka KJ, Le Romancer M, Wauters N, Jacquet S. 2017. Deciphering the virus-to-prokaryote ratio (VPR): insights into virus-host relationships in a variety of ecosystems. Biol Rev Camb Philos Soc 92:1081–1100. https://doi.org/10.1111/brv.12271.
3. Gromov BV. 1983. Cyanophages. Ann Microbiol (Paris) 134b:43–59. https://doi.org/10.1016/s0769-2609(83)80096-9.
4. Muhling M, Fuller NJ, Millard A, Somerfield PJ, Marie D, Wilson WH, Scanlan DJ, Post AF, Joint I, Mann NH. 2005. Genetic diversity of marine *Synechococcus* and co-occurring cyanophage communities: evidence for viral control of phytoplankton. Environ Microbiol 7:499–508. https://doi.org/10.1111/j.1462-2920.2005.00713.x.
5. Schirrmeister BE, Gugger M, Donoghue PCJ. 2015. Cyanobacteria and the great oxidation event: evidence from genes and fossils. Palaeontology 58:769–785. https://doi.org/10.1111/pala.12178.

6. Knoll AH. 2008. Cyanobacteria and earth history, p 1–19, The Cyanobacteria: molecular biology genomics and evolution. Caister Academic Press, Norfolk.
7. Flombaum P, Gallegos JL, Gordillo RA, Rincon J, Zabala LL, Jiao N, Karl DM, Li WK, Lomas MW, Veneziano D, Vera CS, Vrugt JA, Martiny AC. 2013. Present and future global distributions of the marine cyanobacteria *Prochlorococcus* and *Synechococcus*. Proc Natl Acad Sci U S A 110:9824–9829. https://doi.org/10.1073/pnas.1307701110.
8. Suttle CA. 2002. Cyanophages and their role in the ecology of cyanobacteria, p 563–589. *In* Whitton BA, Potts M (ed), The ecology of cyanobacteria: their diversity in time and space. Springer Netherlands, Dordrecht.
9. Puxty RJ, Millard AD, Evans DJ, Scanlan DJ. 2016. Viruses inhibit CO_2 fixation in the most abundant phototrophs on Earth. Curr Biol 26:1585–1589. https://doi.org/10.1016/j.cub.2016.04.036.
10. Suttle CA. 2007. Marine viruses: major players in the global ecosystem. Nat Rev Microbiol 5:801–812. https://doi.org/10.1038/nrmicro1750.
11. Jover LF, Effler TC, Buchan A, Wilhelm SW, Weitz JS. 2014. The elemental composition of virus particles: implications for marine biogeochemical cycles. Nat Rev Microbiol 12:519–528. https://doi.org/10.1038/nrmicro3289.
12. Mann NH, Clokie MRJ. 2012. Cyanophages, p 535–557. *In* Whitton BA (ed), Ecology of cyanobacteria II: their diversity in space and time. Springer Netherlands, Dordrecht.
13. Paerl HW, Otten TG. 2013. Harmful cyanobacterial blooms: causes, consequences, and controls. Microb Ecol 65:995–1010. https://doi.org/10.1007/s00248-012-0159-y.
14. de Oliveira Santos L, Guedes IA, Azevedo S, Pacheco ABF. 2021. Occurrence and diversity of viruses associated with cyanobacterial communities in a Brazilian freshwater reservoir. Braz J Microbiol 52:773–785. https://doi.org/10.1007/s42770-021-00473-8.
15. Walker PJ, Siddell SG, Lefkowitz EJ, Mushegian AR, Adriaenssens EM, Alfenas-Zerbini P, Davison AJ, Dempsey DM, Dutilh BE, García ML, Harrach B, Harrison RL, Hendrickson RC, Junglen S, Knowles NJ, Krupovic M, Kuhn JH, Lambert AJ, Łobocka M, Nibert ML, Oksanen HM, Orton RJ, Robertson DL, Rubino L, Sabanadzovic S, Simmonds P, Smith DB, Suzuki N, Van Dooerslaer K, Vandamme A-M, Varsani A, Zerbini FM. 2021. Changes to virus taxonomy and to the International Code of Virus Classification and Nomenclature ratified by the International Committee on Taxonomy of Viruses (2021). Arch Virol 166:2633–2648. https://doi.org/10.1007/s00705-021-05156-1.
16. Gao EB, Yuan XP, Li RH, Zhang QY. 2009. Isolation of a novel cyanophage infectious to the filamentous cyanobacterium *Planktothrix agardhii* (Cyanophyceae) from Lake Donghu, China. Aquat Microb Ecol 54:163–170. https://doi.org/10.3354/ame01266.
17. Zhang D, You F, He Y, Te SH, Gin KY. 2020. Isolation and characterization of the first freshwater cyanophage infecting *Pseudanabaena*. J Virol 94:e00682-20. https://doi.org/10.1128/JVI.00682-20.
18. Wolk CP, Ernst A, Elhai J. 1994. Heterocyst metabolism and development, p 769–823. *In* Bryant DA (ed), The molecular biology of cyanobacteria. Springer Netherlands, Dordrecht.
19. Kaneko T, Nakamura Y, Wolk CP, Kuritz T, Sasamoto S, Watanabe A, Iriguchi M, Ishikawa A, Kawashima K, Kimura T, Kishida Y, Kohara M, Matsumoto M, Matsuno A, Muraki A, Nakazaki N, Shimpo S, Sugimoto M, Takazawa M, Yamada M, Yasuda M, Tabata S. 2001. Complete genomic sequence of the filamentous nitrogen-fixing cyanobacterium *Anabaena* sp. strain PCC 7120. DNA Res 8:205–213. https://doi.org/10.1093/dnares/8.5.205.
20. Elhai J, Wolk CP. 1988. Conjugal transfer of DNA to cyanobacteria. Methods Enzymol 167:747–754. https://doi.org/10.1016/0076-6879(88)67086-8.
21. Thiel T, Poo H. 1989. Transformation of a filamentous cyanobacterium by electroporation. J Bacteriol 171:5743–5746. https://doi.org/10.1128/jb.171.10.5743-5746.1989.
22. Cai YP, Wolk CP. 1990. Use of a conditionally lethal gene in *Anabaena* sp. strain PCC 7120 to select for double recombinants and to entrap insertion sequences. J Bacteriol 172:3138–3145. https://doi.org/10.1128/jb.172.6.3138-3145.1990.
23. Niu TC, Lin GM, Xie LR, Wang ZQ, Xing WY, Zhang JY, Zhang CC. 2019. Expanding the potential of CRISPR-Cpf1-based genome editing technology in the cyanobacterium *Anabaena* PCC 7120. ACS Synth Biol 8:170–180. https://doi.org/10.1021/acssynbio.8b00437.
24. Borthakur D, Haselkorn R. 1989. Tn5 mutagenesis of *Anabaena* sp. strain PCC 7120: isolation of a new mutant unable to grow without combined nitrogen. J Bacteriol 171:5759–5761. https://doi.org/10.1128/jb.171.10.5759-5761.1989.
25. Kozyakov SY. 1977. Cyanophages of the series A(L) specific for the blue-green alga *Anabaena* variabilis. Exp Algol Biol Sci Res: 151–175.
26. Hu NT, Thiel T, Giddings TH, Jr, Wolk CP. 1981. New *Anabaena* and *Nostoc* cyanophages from sewage settling ponds. Virology 114:236–246. https://doi.org/10.1016/0042-6822(81)90269-5.
27. Chenard C, Wirth JF, Suttle CA. 2016. Viruses infecting a freshwater filamentous cyanobacterium (*Nostoc* sp.) encode a functional CRISPR array and a proteobacterial DNA polymerase B. mBio 7:e00667-16. https://doi.org/10.1128/mBio.00667-16.
28. Xiong Z, Wang Y, Dong Y, Zhang Q, Xu X. 2019. Cyanophage A-1(L) adsorbs to lipopolysaccharides of *Anabaena* sp. strain PCC 7120 via the tail protein lipopolysaccharide-interacting protein (ORF36). J Bacteriol 201:9824–9834. https://doi.org/10.1128/JB.00516-18.
29. Wood WB. 1980. Bacteriophage T4 morphogenesis as a model for assembly of subcellular structure. Q Rev Biol 55:353–367. https://doi.org/10.1086/411980.
30. Leiman PG, Kanamaru S, Mesyanzhinov VV, Arisaka F, Rossmann MG. 2003. Structure and morphogenesis of bacteriophage T4. Cell Mol Life Sci 60:2356–2370. https://doi.org/10.1007/s00018-003-3072-1.
31. Suhanovsky MM, Teschke CM. 2015. Nature's favorite building block: deciphering folding and capsid assembly of proteins with the HK97-fold. Virology 479–480:487–497. https://doi.org/10.1016/j.virol.2015.02.055.
32. Prasad BVV, Schmid MF. 2012. Principles of virus structural organization, p 17–47. *In* Rossmann MG, Rao VB (ed), Viral molecular machines. Springer US, Boston, MA.
33. avorite building block: decipheringQin L, Fokine A, O'Donnell E, Rao VB, Rossmann MG. 2010. Structure of the small outer capsid protein, Soc: a clamp for stabilizing capsids of T4-like phages. J Mol Biol 395:728–741. https://doi.org/10.1016/j.jmb.2009.10.007.
34. Zhang X, Guo HT, Jin L, Czornyj E, Hodes A, Hui WH, Nieh AW, Miller JF, Zhou ZH. 2013. A new topology of the HK97-like fold revealed in *Bordetella* bacteriophage by cryo-EM at 3.5 angstrom resolution. Elife 2:e01299. https://doi.org/10.7554/eLife.01299.
35. Yang F, Forrer P, Dauter Z, Conway JF, Cheng N, Cerritelli ME, Steven AC, Pluckthun A, Wlodawer A. 2000. Novel fold and capsid-binding properties of the lambda-phage display platform protein gpD. Nat Struct Biol 7:230–237. https://doi.org/10.1038/73347.
36. Jin H, Jiang YL, Yang F, Zhang JT, Li WF, Zhou K, Ju J, Chen Y, Zhou CZ. 2019. Capsid structure of a freshwater cyanophage *Siphoviridae* Mic1. Structure 27:1508–1516. https://doi.org/10.1016/j.str.2019.07.003.
37. Wikoff WR, Liljas L, Duda RL, Tsuruta H, Hendrix RW, Johnson JE. 2000. Topologically linked protein rings in the bacteriophage HK97 capsid. Science 289:2129–2133. https://doi.org/10.1126/science.289.5487.2129.
38. Guo F, Liu Z, Fang PA, Zhang Q, Wright ET, Wu W, Zhang C, Vago F, Ren Y, Jakana J, Chiu W, Serwer P, Jiang W. 2014. Capsid expansion mechanism of bacteriophage T7 revealed by multistate atomic models derived from cryo-EM reconstructions. Proc Natl Acad Sci U S A 111:E4606–4614. https://doi.org/10.1073/pnas.1407020111.
39. Hryc CF, Chen DH, Afonine PV, Jakana J, Wang Z, Haase-Pettingell C, Jiang W, Adams PD, King JA, Schmid MF, Chiu W. 2017. Accurate model annotation of a near-atomic resolution cryo-EM map. Proc Natl Acad Sci U S A 114:3103–3108. https://doi.org/10.1073/pnas.1621152114.
40. Zhao HY, Li KP, Lynn AY, Aron KE, Yu GM, Jiang W, Tang L. 2017. Structure of a headful DNA-packaging bacterial virus at 2.9 angstrom resolution by electron cryo-microscopy. Proc Natl Acad Sci U S A 114:3601–3606. https://doi.org/10.1073/pnas.1615025114.
41. Wang Z, Hardies SC, Fokine A, Klose T, Jiang W, Cho BC, Rossmann MG. 2018. Structure of the marine siphovirus TW1: evolution of capsid-stabilizing proteins and tail spikes. Structure 26:238–248. https://doi.org/10.1016/j.str.2017.12.001.
42. Bayfield OW, Klimuk E, Winkler DC, Hesketh EL, Chechik M, Cheng N, Dykeman EC, Minakhin L, Ranson NA, Severinov K, Steven AC, Antson AA. 2019. Cryo-EM structure and in vitro DNA packaging of a thermophilic virus with supersized T=7 capsids. Proc Natl Acad Sci U S A 116:3556–3561. https://doi.org/10.1073/pnas.1813204116.
43. Effantin G, Boulanger P, Neumann E, Letellier L, Conway JF. 2006. Bacteriophage T5 structure reveals similarities with HK97 and T4 suggesting evolutionary relationships. J Mol Biol 361:993–1002. https://doi.org/10.1016/j.jmb.2006.06.081.
44. Chen Z, Sun L, Zhang Z, Fokine A, Padilla-Sanchez V, Hanein D, Jiang W, Rossmann MG, Rao VB. 2017. Cryo-EM structure of the bacteriophage T4 isometric head at 3.3-Å resolution and its relevance to the assembly of icosahedral viruses. Proc Natl Acad Sci U S A 114:E8184–E8193. https://doi.org/10.1073/pnas.1708483114.
45. Choi KH, McPartland J, Kaganman I, Bowman VD, Rothman-Denes LB, Rossmann MG. 2008. Insight into DNA and protein transport in double-

stranded DNA viruses: the structure of bacteriophage N4. J Mol Biol 378:726–736. https://doi.org/10.1016/j.jmb.2008.02.059.
46. Grose JH, Belnap DM, Jensen JD, Mathis AD, Prince JT, Merrill BD, Burnett SH, Breakwell DP. 2014. The genomes, proteomes, and structures of three novel phages that infect the *Bacillus cereus* group and carry putative virulence factors. J Virol 88:11846–11860. https://doi.org/10.1128/JVI.01364-14.
47. Podgorski J, Calabrese J, Alexandrescu L, Jacobs-Sera D, Pope W, Hatfull G, White S. 2020. Structures of three actinobacteriophage capsids: roles of symmetry and accessory proteins. Viruses 12:294. https://doi.org/10.3390/v12030294.
48. Bamford DH, Grimes JM, Stuart DI. 2005. What does structure tell us about virus evolution? Curr Opin Struct Biol 15:655–663. https://doi.org/10.1016/j.sbi.2005.10.012.
49. Baker ML, Jiang W, Rixon FJ, Chiu W. 2005. Common ancestry of herpesviruses and tailed DNA bacteriophages. J Virol 79:14967–14970. https://doi.org/10.1128/JVI.79.23.14967-14970.2005.
50. Holm L. 2020. DALI and the persistence of protein shape. Protein Sci 29:128–140. https://doi.org/10.1002/pro.3749.
51. Hrebík D, Štveráková D, Škubník K, Füzik T, Pantůček R, Plevka P. 2019. Structure and genome ejection mechanism of *Staphylococcus aureus* phage P68. Sci Adv 5:eaaw7414. https://doi.org/10.1126/sciadv.aaw7414.
52. Stone NP, Demo G, Agnello E, Kelch BA. 2019. Principles for enhancing virus capsid capacity and stability from a thermophilic virus capsid structure. Nat Commun 10:4471. https://doi.org/10.1038/s41467-019-12341-z.
53. Ignatiou A, Brasiles S, El Sadek Fadel M, Burger J, Mielke T, Topf M, Tavares P, Orlova EV. 2019. Structural transitions during the scaffolding-driven assembly of a viral capsid. Nat Commun 10:4840. https://doi.org/10.1038/s41467-019-12790-6.
54. Huet A, Conway JF, Letellier L, Boulanger P. 2010. In vitro assembly of the T=13 procapsid of bacteriophage T5 with its scaffolding domain. J Virol 84:9350–9358. https://doi.org/10.1128/JVI.00942-10.
55. Zhou ZH, Chiou J. 2015. Protein chainmail variants in dsDNA viruses. AIMS Biophys 2:200–218. https://doi.org/10.3934/biophy.2015.2.200.
56. Huet A, Duda RL, Boulanger P, Conway JF. 2019. Capsid expansion of bacteriophage T5 revealed by high resolution cryo-electron microscopy. Proc Natl Acad Sci U S A 116:21037–21046. https://doi.org/10.1073/pnas.1909645116.
57. Lander GC, Evilevitch A, Jeembaeva M, Potter CS, Carragher B, Johnson JE. 2008. Bacteriophage lambda stabilization by auxiliary protein gpD: timing, location, and mechanism of attachment determined by cryo-EM. Structure 16:1399–1406. https://doi.org/10.1016/j.str.2008.05.016.
58. Kizziah JL, Manning KA, Dearborn AD, Wall EA, Klenow L, Hill RLL, Spilman MS, Stagg SM, Christie GE, Dokland T. 2017. Cleavage and structural transitions during maturation of *Staphylococcus aureus* bacteriophage 80alpha and SaPI1 capsids. Viruses 9:384. https://doi.org/10.3390/v9120384.
59. Liu X, Zhang Q, Murata K, Baker ML, Sullivan MB, Fu C, Dougherty MT, Schmid MF, Osburne MS, Chisholm SW, Chiu W. 2010. Structural changes in a marine podovirus associated with release of its genome into *Prochlorococcus*. Nat Struct Mol Biol 17:830–836. https://doi.org/10.1038/nsmb.1823.
60. Gipson P, Baker ML, Raytcheva D, Haase-Pettingell C, Piret J, King JA, Chiu W. 2014. Protruding knob-like proteins violate local symmetries in an icosahedral marine virus. Nat Commun 5:4278–4288. https://doi.org/10.1038/ncomms5278.
61. Baker ML, Hryc CF, Zhang Q, Wu W, Jakana J, Haase-Pettingell C, Afonine PV, Adams PD, King JA, Jiang W, Chiu W. 2013. Validated near-atomic resolution structure of bacteriophage epsilon15 derived from cryo-EM and modeling. Proc Natl Acad Sci U S A 110:12301–12306. https://doi.org/10.1073/pnas.1309947110.
62. Duda RL, Hendrix RW, Huang WM, Conway JF. 2006. Shared architecture of bacteriophage SPO1 and herpesvirus capsids. Curr Biol 16:R11–13. https://doi.org/10.1016/j.cub.2005.12.023.
63. Stroupe ME, Brewer TE, Sousa DR, Jones KM. 2014. The structure of *Sinorhizobium meliloti* phage PhiM12, which has a novel T=19l triangulation number and is the founder of a new group of T4-superfamily phages. Virology 450–451:205–212. https://doi.org/10.1016/j.virol.2013.11.019.
64. Fokine A, Kostyuchenko VA, Efimov AV, Kurochkina LP, Sykilinda NN, Robben J, Volckaert G, Hoenger A, Chipman PR, Battisti AJ, Rossmann MG, Mesyanzhinov VV. 2005. A three-dimensional cryo-electron microscopy structure of the bacteriophage phiKZ head. J Mol Biol 352:117–124. https://doi.org/10.1016/j.jmb.2005.07.018.
65. Effantin G, Hamasaki R, Kawasaki T, Bacia M, Moriscot C, Weissenhorn W, Yamada T, Schoehn G. 2013. Cryo-electron microscopy three-dimensional structure of the jumbo phage PhiRSL1 infecting the phytopathogen *Ralstonia solanacearum*. Structure 21:298–305. https://doi.org/10.1016/j.str.2012.12.017.
66. Hua J, Huet A, Lopez CA, Toropova K, Pope WH, Duda RL, Hendrix RW, Conway JF. 2017. Capsids and genomes of jumbo-sized bacteriophages reveal the evolutionary reach of the HK97 fold. mBio 8:e01579-17. https://doi.org/10.1128/mBio.01579-17.
67. Gonzalez B, Monroe L, Li K, Yan R, Wright E, Walter T, Kihara D, Weintraub ST, Thomas JA, Serwer P, Jiang W. 2020. Phage G structure at 6.1 Å resolution, condensed DNA, and host identity revision to a *Lysinibacillus*. J Mol Biol 432:4139–4153. https://doi.org/10.1016/j.jmb.2020.05.016.
68. Zandi R, Reguera D. 2005. Mechanical properties of viral capsids. Phys Rev E Stat Nonlin Soft Matter Phys 72:e021917. https://doi.org/10.1103/PhysRevE.72.021917.
69. Duda RL. 1998. Protein chainmail: catenated protein in viral capsids. Cell 94:55–60. https://doi.org/10.1016/s0092-8674(00)81221-0.
70. Parent KN, Khayat R, Tu LH, Suhanovsky MM, Cortines JR, Teschke CM, Johnson JE, Baker TS. 2010. P22 coat protein structures reveal a novel mechanism for capsid maturation: stability without auxiliary proteins or chemical crosslinks. Structure 18:390–401. https://doi.org/10.1016/j.str.2009.12.014.
71. Zhou ZH, Hui WH, Shah S, Jih J, O'Connor CM, Sherman MB, Kedes DH, Schein S. 2014. Four levels of hierarchical organization, including noncovalent chainmail, brace the mature tumor herpesvirus capsid against pressurization. Structure 22:1385–1398. https://doi.org/10.1016/j.str.2014.05.019.
72. D'Lima NG, Teschke CM. 2015. A molecular staple: D-Loops in the I domain of bacteriophage P22 coat protein make important intercapsomer contacts required for procapsid assembly. J Virol 89:10569–10579. https://doi.org/10.1128/JVI.01629-15.
73. Zheng SQ, Palovcak E, Armache JP, Verba KA, Cheng Y, Agard DA. 2017. MotionCor2: anisotropic correction of beam-induced motion for improved cryo-electron microscopy. Nat Methods 14:331–332. https://doi.org/10.1038/nmeth.4193.
74. Rohou A, Grigorieff N. 2015. CTFFIND4: fast and accurate defocus estimation from electron micrographs. J Struct Biol 192:216–221. https://doi.org/10.1016/j.jsb.2015.08.008.
75. Scheres SH. 2012. RELION: implementation of a Bayesian approach to cryo-EM structure determination. J Struct Biol 180:519–530. https://doi.org/10.1016/j.jsb.2012.09.006.
76. Emsley P, Lohkamp B, Scott WG, Cowtan K. 2010. Features and development of Coot. Acta Crystallogr D Biol Crystallogr 66:486–501. https://doi.org/10.1107/S0907444910007493.
77. Liebschner D, Afonine PV, Baker ML, Bunkoczi G, Chen VB, Croll TI, Hintze B, Hung LW, Jain S, McCoy AJ, Moriarty NW, Oeffner RD, Poon BK, Prisant MG, Read RJ, Richardson JS, Richardson DC, Sammito MD, Sobolev OV, Stockwell DH, Terwilliger TC, Urzhumtsev AG, Videau LL, Williams CJ, Adams PD. 2019. Macromolecular structure determination using X-rays, neutrons and electrons: recent developments in Phenix. Acta Crystallogr D Struct Biol 75:861–877. https://doi.org/10.1107/S2059798319011471.
78. Williams CJ, Headd JJ, Moriarty NW, Prisant MG, Videau LL, Deis LN, Verma V, Keedy DA, Hintze BJ, Chen VB, Jain S, Lewis SM, Arendall WB, 3rd, Snoeyink J, Adams PD, Lovell SC, Richardson JS, Richardson DC. 2018. MolProbity: more and better reference data for improved all-atom structure validation. Protein Sci 27:293–315. https://doi.org/10.1002/pro.3330.
79. Pettersen EF, Goddard TD, Huang CC, Couch GS, Greenblatt DM, Meng EC, Ferrin TE. 2004. UCSF Chimera - a visualization system for exploratory research and analysis. J Comput Chem 25:1605–1612. https://doi.org/10.1002/jcc.20084.
80. Pettersen EF, Goddard TD, Huang CC, Meng EC, Couch GS, Croll TI, Morris JH, Ferrin TE. 2021. UCSF ChimeraX: structure visualization for researchers, educators, and developers. Protein Sci 30:70–82. https://doi.org/10.1002/pro.3943.
81. Laskowski RA, Jabłońska J, Pravda L, Vařeková RS, Thornton JM. 2018. PDBsum: structural summaries of PDB entries. Protein Sci 27:129–134. https://doi.org/10.1002/pro.3289.
82. Krissinel E, Henrick K. 2007. Inference of macromolecular assemblies from crystalline state. J Mol Biol 372:774–797. https://doi.org/10.1016/j.jmb.2007.05.022.